J. Fluid Mech. (2000), *vol.* 412, *pp.* 197–225. Printed in the United Kingdom

A numerical study of viscoelastic effects in chaotic mixing between eccentric cylinders

By YURUN FAN, ROGER I. TANNER AND NHAN PHAN-THIEN†

Department of Mechanical and Mechatronic Engineering, The University of Sydney, NSW 2006, Australia

(Received 1 April 1999 and in revised form 20 December 1999)

In this paper, we are concerned with the effect of fluid elasticity and shear-thinning viscosity on the chaotic mixing of the flow between two eccentric, alternately rotating cylinders. We employ the well-developed *h-p* finite element method to achieve a high accuracy and efficiency in calculating steady solutions, and a full unsteady algorithm for creeping viscoelastic flows to study the transient process in this periodic viscoelastic flow. Since the distribution of periodic points of the viscoelastic flow is not symmetric, we have developed a domain-search algorithm based on Newton iteration for locating the periodic points. With the piecewise-steady approximation, our computation for the upper-convected Maxwell fluid predicts no noticeable changes of the advected coverage of a passive tracer from Newtonian flow, with elasticity levels up to a Deborah number of 1.0. The stretching of the fluid elements, quantified by the geometrical mean of the spatial distribution, remains exponential up to a Deborah number of 6.0, with only slight changes from Newtonian flow. On the other hand, the shear-thinning viscosity, modelled by the Carreau equation, has a large impact on both the advection of a passive tracer and the mean stretching of the fluid elements. The creeping, unsteady computations show that the transient period of the velocity is much shorter than the transient period of the stress, and from a pragmatic point of view, this transient process caused by stress relaxation due to sudden switches of the cylinder rotation can be neglected for predicting the advective mixing in this time-periodic flow. The periodic points found up to second order and their eigenvalues are indeed very informative in understanding the chaotic mixing patterns and the qualitative changes of the mean stretching of the fluid elements. The comparison between our computations and those of Niederkorn & Ottino (1993) reveals the importance of reducing the discretization error in the computation of chaotic mixing. The causes of the discrepancy between our prediction of the tracer advection and Niederkorn & Ottino's (1993) experiment are discussed, in which the influence of the shear-thinning first normal stress difference is carefully examined. The discussion leads to questions on whether small elasticity of the fluid has a large effect on the chaotic mixing in this periodic flow.

1. Introduction

Mixing of non-Newtonian fluids is common in a variety of industrial applications such as the processing of polymers, food and biochemical materials. In recent years

† Present address: Department of Mechanical and Production Engineering, National University of Singapore, Singapore 119260.

there have been considerable advances in understanding the mechanism of advective mixing of viscous fluids in the Stokes flow regime. It is now well established that in steady two-dimensional flows, the mixing is regular while in unsteady two-dimensional flows there is a good chance that the mixing is chaotic in some regions of the flow (Aref & Balachandar 1986; Ottino 1989). From a kinematic point of view, advective mixing, not including diffusion, is nothing more than stretching and folding of the fluid lines and surfaces; in regular regions the stretching rate is linear for a long time, while in chaotic regions it increases exponentially. Therefore one of the primary means of increasing mixing efficiency is to enhance and control the chaotic region in the flow, and it is obviously of vital importance to understand the mechanism and to estimate the effect of the fluid rheology on the character of chaotic advection.

There are a few model mixers amenable to detailed investigations both by experimentation and computation; one of them is the eccentric helical annular mixer (EHAM). This mixer has a continuous input–output with no sharp edges – an important advantage that is desirable for some 'delicate' fluids such as bio-materials (see Kusch & Ottino 1992). The two-dimensional problem closely related to the EHAM mixer is the chaotic mixing between eccentric cylinders which has been extensively analysed in the Stokes regime (Chaiken *et al.* 1986; Aref & Balachandar 1986; Swanson & Ottino 1990; Muzzio, Swanson & Ottino 1991). The smooth boundaries and the existence of analytical solutions (e.g. Wannier 1950) make this flow an ideal test case for numerical simulations. For Newtonian fluid, an excellent agreement between the experimentally observed and the theoretically predicted mixing patterns has been demonstrated (Swanson & Ottino 1990).

The experimental and computational investigations of Niederkorn & Ottino (1993, 1994) have addressed two non-Newtonian properties that influence chaotic mixing in the eccentric annulus, namely fluid elasticity and shear-thinning of the fluid viscosity. They found that relatively small deviations of the velocity field from the Newtonian kinematics can have a large impact on the chaotically advected patterns. It is noteworthy that in their study on viscoelastic flow with low levels of elasticity, some astonishingly perfect matches of the tracer coverage between the experiment with Boger fluids and the computation using the upper-convected Maxwell (UCM) constitutive equation have been observed, although the discretization error of the velocity field in their calculation is rather large. Chaotic advection in the eccentric cylindrical geometry is accomplished by alternately rotating the inner and outer cylinders. A square-wave form of the modulation was adopted in Niederkorn & Ottino's investigations. The key assumption in their computation is to approximate the unsteady flow by a sequence of piecewise-steady flows. The piecewise-steady assumption is valid for Newtonian creeping flows where the fluid inertia is negligible. However, in the case of viscoelastic flows, because of the timescales in the constitutive equations (the stress relaxation process), the transient stress field may have an important influence on the velocity field, especially when the rotation changes suddenly from one cylinder to another.

Based on a perturbation solution for UCM fluid with low levels of elasticity, Kumar & Homsy (1996) applied the geometric theory of Kaper & Wiggins (1993) to analyse the effect of viscoelasticity on the area over which chaotic advection occurs; with slow, continuous modulations of the cylinder rotations, their quasi-steady approximation is more justified. They indicated that the mechanism responsible for the area changes is a modified pressure gradient in the angular direction, which appears due to the first normal stress differences caused by shearing. However, the magnitude of the correction terms in their perturbation solution is rather large, compared to the base solution.

Numerical simulations are inherently subject to approximation errors. A clear error analysis of the validity of the numerical simulation of advective mixing has been given in the pioneering investigation of Souvaliotis, Jana & Ottino (1995). The study indicates that the errors, defined as the distance between the exact and the calculated fluid particle locations, are mainly composed of the discretization errors of the velocity field from finite element or finite difference solutions, and the time integration errors. In general, these errors behave like differential material lines, and the cumulative or global errors, at any given time, are the sum of all the previously introduced errors as they have grown within the flow field. One important fact found is that the errors tend to align with the streamlines in regular regions and with the manifolds of the hyperbolic points in chaotic regions. As a consequence, even though exact and calculated trajectories diverge exponentially fast in the chaotic regions, the overall mixing patterns (e.g. the dye striations, the type of low-order periodic points, etc.) are reproduced at least qualitatively. This suggests that the accuracy requirement for the velocity field is not as stringent as the exponential stretching of chaotic mixing seems to suggest.

Our objective in the present study is to develop accurate and efficient numerical methods to investigate the impact of the fluid elasticity, the shear-rate-dependent viscosity and the transient process on the mixing characteristics in the time-periodic flow between eccentric cylinders. Especially, in view of the error estimations reported in Niederkorn & Ottino's work, we believe it is necessary to reduce the discretization error of the velocity field before proceeding confidently with analysing the advective mixing. To keep the investigation reasonably focused, the same geometric configuration and operating conditions as Niederkorn & Ottino's investigations are adopted; only the case of counter-rotating cylinders is considered. Shear-rate-dependent viscosity of the fluid is modelled by the Carreau equation and the field equations are solved by the mixed finite element method. Viscoelasticity of the fluid is modelled by the UCM and Oldroyd-B constitutive equations. A Galerkin/least-square finite element method, developed by the authors, is employed to solve the steady field equations of the viscoelastic flows. Accuracy and convergence of the algorithms are demonstrated by increasing the finite element interpolation orders (the so-called *p*-extension), checking the results with the analytic solutions for Newtonian flow, and comparing with accurate numerical solutions for viscoelastic flow in the literature. A full unsteady finite element algorithm for creeping, viscoelastic flows is developed and used to examine the effects of the transient process on this time-periodic flows.

Our approach in analysing the advective chaotic mixing includes plotting the coverage of a passive tracer, evaluating the mean stretching of the fluid elements, and searching for and characterizing the periodic points. Since the distribution of the periodic points is not symmetric in the viscoelastic flow, a new domain-search algorithm for locating the periodic points is proposed and verified. Finally, we discuss the causes for the discrepancy between our prediction of the passive-tracer coverage and the experiment of Niederkorn & Ottino (1993). In particular, we question the conclusion that a small amount of elasticity of the fluid has a large effect on the chaotic mixing in the flow between eccentric cylinders.

2. Model mixing problem

The flow domain is confined between two eccentric cylinders with parallel axes displaced by a distance e. The radii of the inner and outer cylinders are R_i and R_o, respectively. The flow geometry is completely specified by a dimensionless gap μ and

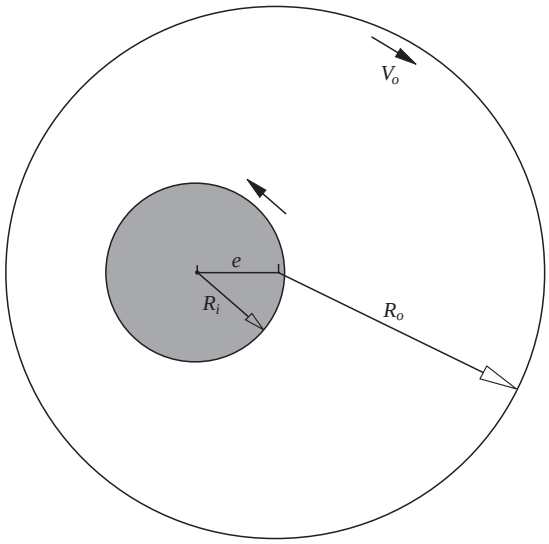

FIGURE 1. Geometric definitions of the problem with $R_i = 1.0$, $R_0 = 3.0$ and $e = 0.9$; $\mu = 2.0$, $\epsilon = 0.45$.

a dimensionless eccentricity ϵ which are defined as

$$\mu = \frac{R_o - R_i}{R_i}, \tag{2.1}$$

$$\epsilon = \frac{e}{R_o - R_i}. \tag{2.2}$$

Figure 1 sketches the typical geometry for $\mu = 2.0$ and $\epsilon = 0.45$ used in the present study; this also has been used in the investigations of Swanson & Ottino (1990), and Niederkorn & Ottino (1993, 1994). Chaotic advection can be created by alternately rotating the inner and outer cylinders with the angular velocities ω_i and ω_o, respectively. In addition, at any one time, only one cylinder is allowed to rotate with a constant angular velocity and the change from one cylinder to another rotating is instantaneous. The movement of the boundaries is thus prescribed by a symmetric, square-wave form:

$$\omega_i(t) = \begin{cases} \omega_i, & 0 \leqslant t \leqslant T/4 \\ 0, & T/4 \leqslant t \leqslant 3T/4 \\ \omega_i, & 3T/4 \leqslant t \leqslant T, \end{cases}$$

$$\omega_o(t) = \begin{cases} 0, & 0 \leqslant t \leqslant T/4 \\ \omega_o, & T/4 \leqslant t \leqslant 3T/4 \\ 0, & 3T/4 \leqslant t \leqslant T, \end{cases}$$

that is, a period T is composed of rotation of the inner cylinder with a constant ω_i for $T/4$, followed by rotation of the outer cylinder with a constant ω_o for $T/2$ and concluding with rotation of the inner cylinder with the same ω_i for $T/4$. The ratio of the angular velocities $|\omega_i/\omega_o|$ is set equal to the ratio of the radii, thus the linear speed is the same for both cylinders. In this investigation we only consider the counter-rotating modulation, hence $\omega_i/\omega_o = -3.0$, corresponding to $V_i = -1.0$ and $V_o = 1.0$. Given ω_i/ω_o, a particular time-periodic flow is characterized by the total

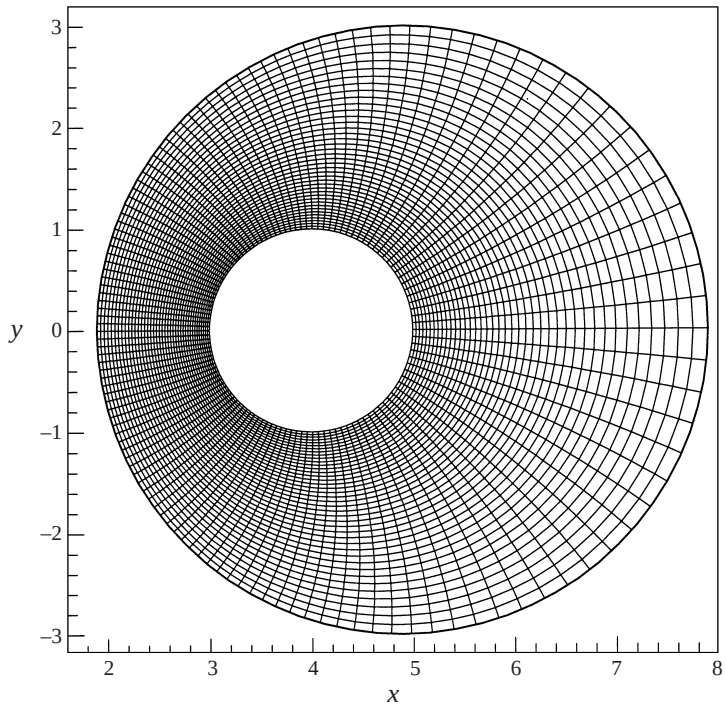

FIGURE 2. Finite element mesh used for the case of $\mu = 2.0$, $\epsilon = 0.45$.

angular displacement of the outer cylinder in a period:

$$\theta = \int_0^T \omega_o \, \mathrm{d}t. \tag{2.3}$$

3. Numerical methods

For the eccentric annulus geometry, the bipolar coordinate system is preferred because of its orthogonality and its ability to fit the boundaries to the coordinate lines. The transformation from the rectangular coordinates (x, y) to the bipolar coordinate system (ξ, ϕ) is defined as

$$x = \frac{a \sinh \xi}{\cosh \xi + \cos \phi}, \quad y = \frac{a \sin \xi}{\cosh \xi + \cos \phi},$$

where a is a geometric parameter based on the eccentricity and the radii,

$$a = \frac{1}{2e}\sqrt{(R_i^2 + R_o^2 - e^2)^2 - 4R_i^2 R_o^2}.$$

The finite element mesh used in this study for the case $\mu = 2.0$, $\epsilon = 0.45$ is shown in figure 2. It consists of 20 radial elements and 60 azimuthal elements. Note that, due to the limitation of the graphics tool used, each element is plotted as four sub-elements.

The numerical simulation of viscoelastic flows still represents a challenging task in terms of accuracy, stability, convergence and demand for computing resources. In this study we use the *h*-*p*-type finite element method to obtain high accuracy and efficiency. It is well-known that high-order finite element methods (namely *p*-refinement) have an exponential convergence rate for smooth problems and a local combination of the *p*-refinement with the *h*-refinement (i.e. mesh refinement) provides a further efficiency

and flexibility (Talwar & Khomami 1992; Fan & Crochet 1995; Fan 1997; Warichet & Legat 1997). The mesh shown in figure 2 may look rather coarse, but the solutions reported later will demonstrate its high accuracy and good convergence property under the *p*-extension process. For the basis functions of the finite element spaces, we adopted a set of hierarchic shape functions proposed by Szabo & Babuska (1991), which are based on Legendre polynomials. In our computations, the velocity and the extra stress are approximated with the same order of polynomials while the pressure is kept one order less than the velocity in order to meet the LBB compatibility condition (see Huilgol & Phan-Thien 1997), the calculation of the lowest order is with the velocity approximated by biquadratic polynomials.

3.1. *FE methods for steady flows of Newtonian and shear-thinning fluids*

The continuity and momentum equations for the isothermal, creeping, steady flows of incompressible fluids are

$$\nabla \cdot \boldsymbol{u} = 0, \tag{3.1}$$

$$-\nabla p + \nabla \cdot \boldsymbol{\tau} = \mathbf{0}, \tag{3.2}$$

where $\boldsymbol{u}$ is the velocity, p the pressure and $\boldsymbol{\tau}$ the extra-stress tensor. For Newtonian fluids,

$$\boldsymbol{\tau} = \eta(\nabla \boldsymbol{u} + \nabla \boldsymbol{u}^T), \tag{3.3}$$

where η is a constant viscosity for isothermal flows and the superscript T denotes the transpose operation.

The model used in this study is the inelastic Carreau model with a zero infinite-shear-rate viscosity (Bird, Armstrong & Hassager 1987):

$$\eta = \eta_0[1 + (\lambda_c \dot{\gamma})^2]^{(n-1)/2}, \tag{3.4}$$

which includes a characteristic viscosity η_0, a timescale λ_c and a power-law index n. This model accounts for the low-shear-rate Newtonian plateau and transition into the power-law region (shear-thinning property with $n < 1$), which are exhibited by most fluids with long chain microstructures. Here, we define $\dot{\gamma} = \sqrt{2 \operatorname{tr} \boldsymbol{D}^2}$ where $\boldsymbol{D} = (\nabla \boldsymbol{u} + \nabla \boldsymbol{u}^T)/2$ is the strain-rate tensor. The transition from the Newtonian plateau to the power-law region occurs when $\lambda_c \dot{\gamma}$ is $O(1)$.

Throughout this study, we use R_i as a characteristic length, and the linear velocity of either cylinder as a characteristic velocity V (note that $\omega_i/\omega_o = R_o/R_i$ is prescribed). The extra stress and pressure are scaled by $\eta V/R_i$, or $\eta_0 V/R_i$ in the case of shear-thinning fluids. The dimensionless constitutive equation for the inelestic Carreau model is

$$\boldsymbol{\tau} = [1 + (C_r \dot{\gamma})^2]^{(n-1)/2}(\nabla \boldsymbol{u} + \nabla \boldsymbol{u}^T), \tag{3.5}$$

where $C_r = \lambda_c V/R_i$, called the Carreau number.

Let Ω be the flow domain and $\partial\Omega$ its boundary. On $\partial\Omega$, the partial boundaries $\partial\Omega_u$, $\partial\Omega_N$ are identified with boundary conditions for the velocity $\boldsymbol{u}$ and the traction force $\boldsymbol{t}$, respectively. The variational formulation for Carreau fluids can be stated as: *Find the set* $(u, p) \in V \times P$ *such that* $\forall \Phi_u \in \mathscr{V}$, $\forall \Phi_p \in \mathscr{P}$,

$$\int_\Omega ([1 + (C_r \dot{\gamma})^2]^{(n-1)/2}(\nabla \boldsymbol{u} + \nabla \boldsymbol{u}^T) : \nabla \Phi_u - p \nabla \cdot \Phi_u) \, \mathrm{d}\Omega = \int_{\partial\Omega_N} \boldsymbol{t} \cdot \Phi_u \, \mathrm{d}\partial\Omega, \tag{3.6}$$

$$\int_\Omega (\nabla \cdot \boldsymbol{u}) \Phi_p \, \mathrm{d}\Omega = 0, \tag{3.7}$$

where $\mathscr{V}, \mathscr{P}$ *denote the function spaces defined on* Ω *and spanned by the basis functions* Φ_u, Φ_p, *for the velocity and pressure, respectively.*

This is a straightforward adaptation of the mixed finite element method for the incompressible Navier–Stokes equations where $C_r = 0$ or $n = 1$. After discretization, the nonlinear set of equations for the unknown variables $\boldsymbol{u}, p$ is solved by the Newton iteration scheme. It was found that, generally, after three iterations the maximum variation $\max\{\delta \boldsymbol{u}, \delta p\}$ is less than 10^{-4}, indicating that this is a very high efficiency algorithm.

3.2. *Finite element methods for steady flows of viscoelastic fluids*

The constitutive equation for viscoelastic fluids considered in this study is the Oldroyd-B model where the extra stress consists of two parts: $\boldsymbol{\tau}_s$ is from the Newtonian solvent, and $\boldsymbol{\tau}_p$ from the polymer which obeys the upper-convected Maxwell (UCM) constitutive equation. The non-dimensional forms of the equations are

$$\boldsymbol{\tau}_s = \beta(\nabla \boldsymbol{u} + \nabla \boldsymbol{u}^T), \tag{3.8}$$

$$\boldsymbol{\tau}_p + D_e \boldsymbol{\tau}_{p(1)} = (1 - \beta)(\nabla \boldsymbol{u} + \nabla \boldsymbol{u}^T), \tag{3.9}$$

with the Deborah number defined as

$$D_e = \lambda V / R_i, \tag{3.10}$$

and the relative Newtonian viscosity as

$$\beta = \frac{\eta_s}{\eta_s + \eta_p}, \tag{3.11}$$

where λ is the fluid relaxation time and η_s, η_p the viscosity contributions from the solvent and polymer, respectively. The subscript (1) stands for the upper-convected derivative defined by

$$\boldsymbol{\tau}_{(1)} = \boldsymbol{u} \cdot \nabla \boldsymbol{\tau} - \boldsymbol{\tau} \cdot \nabla \boldsymbol{u} - \nabla \boldsymbol{u}^T \cdot \boldsymbol{\tau}. \tag{3.12}$$

If $\beta = 0$ *then* $\tau = \tau_p$ *and the model reduces to the UCM model.*

In the field of finite element methods for differential constitutive equations, it is now a common practice to use the Galerkin weighted residual method for the momentum and continuity equations, and the streamline upwind Petrov–Galerkin (SUPG) technique (Brooks & Hughes 1982) for the constitutive equation. The latter is due to the hyperbolic character with respect to the stress variables. However, in the case of a small contribution of the solvent stress, $\beta \ll 1$, or the UCM model, $\beta = 0$, the algorithms are often confronted with instability or the loss of convergence with respect to the mesh refinement at a moderate level of fluid elasticity. One explanation is that the momentum equation, which, together with the incompressibility constraint, forms a saddle-point problem, loses its explicit elliptic character for the velocity variable in such cases. This argument has led to several stable and convergent algorithms such as the explicitly elliptic momentum equation formulation (EEME, King *et al.* 1988), the elastic-viscous stress split formulation (EVSS, Rajagopalan, Armstrong & Brown 1990) and the adaptive viscoelastic stress splitting formulation (AVSS, Sun, Phan-Thien & Tanner 1996). Another approach is to introduce a least-square perturbation to stabilize the algorithm. To the usual Galerkin formulation, the Galerkin/least-square methods (Hughes, Franca & Hublert 1989; Franca & Frey 1992; Behr, Franca & Tezduyar 1993) add some terms that are the functions of the residuals of the Euler–Lagrange equations. The added perturbation terms are designed to enhance the stability of the original Galerkin method while preserving the consistency with the

exact solution. In the field of viscoelastic flows, the Galerkin/least-square methods include the discrete EVSS (DEVSS) method proposed by Guénette & Fortin (1995) and the MIX1 method proposed by the authors. The MIX1 method has been demonstrated to be superior to the DEVSS method in the sense that it does not need to solve for the strain-rate tensor while it has the same level of accuracy and stability as the DEVSS method; the reader is referred to Fan, Tanner & Phan-Thien (1999) for details.

The variational formulation, called MIX1, for the steady viscoelastic flow is stated as follows:

Find the set $(\tau, u, p) \in \mathscr{T} \times \mathscr{V} \times \mathscr{P}$ *such that* $\forall \Phi_u \in \mathscr{V}$, $\forall \Phi_p \in \mathscr{P}$, $\forall \Phi_\tau \in \mathscr{T}$,

$$\int_\Omega (\beta(\nabla \boldsymbol{u} + \nabla \boldsymbol{u}^T) + \boldsymbol{\tau}_p) : \nabla \Phi_u - p \nabla \cdot \Phi_u) \, \mathrm{d}\Omega + \int_\Omega \alpha_c (\nabla \cdot \boldsymbol{u})(\nabla \cdot \Phi_u) \, \mathrm{d}\Omega = \int_{\partial \Omega_N} \boldsymbol{t} \cdot \Phi_u \, \mathrm{d}\partial\Omega, \tag{3.13}$$

$$\int_\Omega (\nabla \cdot \boldsymbol{u}) \Phi_p \, \mathrm{d}\Omega = 0, \tag{3.14}$$

$$\int_\Omega (\boldsymbol{\tau}_p + D_e \boldsymbol{\tau}_{p(1)} - (1 - \beta)(\nabla \boldsymbol{u} + \nabla \boldsymbol{u}^T)) : (\Phi_\tau + k \boldsymbol{u} \cdot \nabla \Phi_\tau) \, \mathrm{d}\Omega = 0, \tag{3.15}$$

where $\mathscr{T}$, $\mathscr{V}$, $\mathscr{P}$ *denote the function spaces defined on* Ω *and spanned by the basis functions* Φ_τ, Φ_u, Φ_p, *for the extra stress, velocity and pressure, respectively.*

In equation (3.13) the term containing α_c is a least-square form of the residual of the continuity equation. This added perturbation term considerably enhances the stability and keeps the convergence property of the original Galerkin algorithm. In creeping viscoelastic flows, the numerical experiments of Fan *et al.* (1999) indicated that the constant α_c has a good stabilization and this performance is insensitive over a relatively large range of α_c (dimensionless values ranging from 1 to 30). In the present study we take $\alpha_c = 1$. Equation (3.15) is the SUPG formulation for the constitutive equation in which we choose the parameter $k = h/v_m$ where h is the element size along the local flow direction and v_m is a mean value of the velocity magnitude over the element. This choice comes from the investigation of Fan & Crochet (1995); it guarantees that the upwind term approaches zero together with the velocity on the stationary walls.

After discretization, the nonlinear set of equations for the unknown variables $\boldsymbol{\tau}_p, \boldsymbol{u}, p$ is solved by the Newton iteration scheme. The calculations were carried out by increasing the Deborah number D_e in steps of 0.5 from zero (Newtonian flow) to a designated value. Generally, after five iterations the maximum variation $\max\{\delta \boldsymbol{\tau}_p, \delta \boldsymbol{u}, \delta p\}$ is less than 10^{-4}, indicative of an excellent convergence behaviour.

3.3. *Finite element methods for creeping unsteady flows of viscoelastic fluids*

Let us consider the basic governing equations. If the fluid inertia is negligible, the only change from steady to unsteady flows takes place in the constitutive equation where the upper-convected derivative contains an additional time derivative:

$$\boldsymbol{\tau}_{p(1)} = \frac{\partial \boldsymbol{\tau}_p}{\partial t} + \boldsymbol{u} \cdot \nabla \boldsymbol{\tau}_p - \boldsymbol{\tau}_p \cdot \nabla \boldsymbol{u} - \nabla \boldsymbol{u}^T \cdot \boldsymbol{\tau}_p. \tag{3.16}$$

This implies that a transient process of the velocity is determined by the transient process of the elastic stress, and also by the transient movement of the boundaries. The local time derivative enable us to devise a simple one-step time-marching algorithm for unsteady viscoelastic flows. This algorithm is semi-implicit and has an accuracy

of $O(\delta t)$ in the time dimension. Letting the superscript n denote the solution at time $n\delta t$, and $n+1$ the solution at time $(n+1)\delta t$, then the algorithm for creeping unsteady viscoelastic flows can be stated as follows.

Given the set $(\tau^n, u^n, p^n) \in \mathscr{T} \times \mathscr{V} \times \mathscr{P}$, *find the set* $(\tau^{n+1}, u^{n+1}, p^{n+1}) \in \mathscr{T} \times \mathscr{V} \times \mathscr{P}$ *such that* $\forall \Phi_u \in \mathscr{V}$, $\forall \Phi_p \in \mathscr{P}$, $\forall \Phi_\tau \in \mathscr{T}$,

$$\int_\Omega ((\beta(\nabla \boldsymbol{u}^{n+1} + \nabla u^{T(n+1)}) + \boldsymbol{\tau}_p^n) : \nabla \Phi_u - p^{n+1} \nabla \cdot \Phi_u)\, \mathrm{d}\Omega + \int_\Omega \alpha_c (\nabla \cdot \boldsymbol{u}^{n+1})(\nabla \cdot \Phi_u)\, \mathrm{d}\Omega = \int_{\partial \Omega_N} \boldsymbol{t}^n \cdot \Phi_u \, \mathrm{d}\partial\Omega \tag{3.17}$$

$$\int_\Omega (\nabla \cdot \boldsymbol{u}^{n+1}) \Phi_p \, \mathrm{d}\Omega = 0 \tag{3.18}$$

$$\int_\Omega \left[\boldsymbol{\tau}_p^{n+1} + D_e \frac{\boldsymbol{\tau}_p^{n+1} - \boldsymbol{\tau}_p^n}{\delta t} + D_e([\boldsymbol{u} \cdot \nabla \boldsymbol{\tau}_p] - [\boldsymbol{\tau}_p \cdot \nabla \boldsymbol{u}] - [\nabla \boldsymbol{u} \cdot \boldsymbol{\tau}_p])^* - (1-\beta)(\nabla \boldsymbol{u}^n + \nabla \boldsymbol{u}^{T n}) \right] : (\Phi_\tau + k \boldsymbol{u}^n \cdot \nabla \Phi_\tau)\, \mathrm{d}\Omega = 0, \tag{3.19}$$

where $\mathscr{T}$, $\mathscr{V}$, $\mathscr{P}$ *denote the function spaces defined on* Ω *and spanned by the basis functions* Φ_τ, Φ_u, Φ_p, *for the extra stress, velocity and pressure, respectively.*

At time $(n+1)\delta t$, the computation is decoupled into the velocity–pressure computation, equations (3.17) and (3.18), and the extra-stress computation, equation (3.19). In two-dimensional flows, the stress tensor $\boldsymbol{\tau}_p$ contains four components $\boldsymbol{\tau}_{p,ij}$ with $\boldsymbol{\tau}_{p,ij} = \boldsymbol{\tau}_{p,ji}$, $i, j = 1, 2$; thus (3.19) expands to three coupled equations with respect to the advection of each components; in the terms denoted by the superscript $*$ in (3.19), the component $\boldsymbol{\tau}_{p,ij}$ is taken at the time $(n+1)\delta t$ while the other components appearing in this equation are taken at the time $n\delta t$.

This decoupled, implicit–explicit algorithm is designed as a compromise between efficiency and stability requirements in the excessively time-consuming computations of unsteady viscoelastic flows. Since the stress $\boldsymbol{\tau}_p$ is explicit in (3.17), the velocity–pressure computation becomes a linear Stokes problem and the coefficients of the finite element equations are independent of the stress and time; thus the LU matrix splitting of the Gauss elimination can be done only once at the start of the computation and stored for back-substitution of later time-marching. The efficiency of computation is thereby greatly improved. However, also due to this feature, the present algorithm can only be applied to fluids with a stress contribution of a Newtonian solvent such as the Oldroyd-B model; the LU matrix splitting corresponding to the term containing α_c was found to be singular, so it is necessary that $\beta > 0$ in (3.17) to (3.19). Note that if we introduce a stress splitting scheme such as the DEVSS method (Guénette & Fortin 1995), this limitation can be removed at the additional expense of solving for the strain-rate variables.

3.4. *Time integration of trajectories*

The trajectory or pathline of a fluid particle can be computed by integrating the equation of motion,

$$\frac{\mathrm{d}\boldsymbol{x}}{\mathrm{d}t} = \boldsymbol{u}(\boldsymbol{x}, t); \quad \boldsymbol{x}_{t=0} = \boldsymbol{X}, \tag{3.20}$$

provided that the velocity field $\boldsymbol{u}$ is given. The time dependence of $\boldsymbol{u}$ is the source of chaotic behaviour in the system, and this dependence is periodic and discontinuous

in the current situation. In the piecewise-steady computations, two steady velocity fields corresponding to the rotation of each cylinder are first computed; through the basis functions of the finite element spaces, the spatial distributions of $\boldsymbol{u}$ are obtained. The second-order Runge–Kutta method is used to integrate (3.20). To determine the appropriate time step, consecutive tests of integrating one particle for one period were performed; at each test the time step was halved and the number of steps was doubled, until the final position of the particle was within the error of 10^{-4} in the (x, y) coordinates.

In the full unsteady computations, the field equation calculation and the particle trajectory integration must be implemented simultaneously. To save CPU time, the time step of the field equations is taken as five times the time step of the trajectory integration, in which $\boldsymbol{u}(\boldsymbol{x}, t)$ is linearly interpolated between the two time-discrete velocity fields. In our computations, typically, 600 time steps of the field equations were employed for the outer cylinder to cover $\theta = 3\pi/2$ and 800 time steps for $\theta = 2\pi$, corresponding to, respectively, 6000 and 8000 time steps of the trajectory integration for one period. This algorithm is found to be reasonably accurate and stable for the current unsteady viscoelastic flows.

A typical experiment is performed by injecting a dyed blob of fluid and advecting the fluid by alternately rotating the cylinders. In our numerical simulation, initially the tracer is represented by an element in the bipolar frame and consists of 10 000 fluid particles; the initial location is in the middle of the smaller gap. This sample number is far from enough to track material surfaces of the tracer due to the exponential rate of the stretching in the flow (Franjione & Ottino 1987). Fortunately, as the study of Muzzio *et al.* (1991) indicated, the mixing pattern has a considerable degree of self-similarity, and folds present in early periods remain throughout the experiment as details are added on a finer and finer scale. Therefore a faithful picture of the dye structure after N_p periods can be produced by plotting all of the tracer positions corresponding to the previous periods.

3.5. *Lineal stretching of fluid elements*

Advective mixing is a result of stretching and folding of fluid elements; therefore the amount of lineal stretching can be used to quantify the efficiency of mixing. To determine the stretching, consider an infinitesimal fluid element attached to an infinitesimal vector of arbitrary initial orientation; the evolution of the vector can be computed if one knows the deformation gradient tensor:

$$\mathrm{d}\boldsymbol{x}(t) = \boldsymbol{F}(t) \cdot \mathrm{d}\boldsymbol{X}, \tag{3.21}$$

where $\mathrm{d}\boldsymbol{X}$ is the initial vector, $\mathrm{d}\boldsymbol{x}$ the deformed vector and $\boldsymbol{F}$ the deformation gradient tensor. This requires solving the evolution equation of $\boldsymbol{F}$,

$$\frac{\mathrm{d}\boldsymbol{F}}{\mathrm{d}t} = (\nabla \boldsymbol{u})^T \cdot \boldsymbol{F}, \quad \boldsymbol{F}_{t=0} = \boldsymbol{I}, \tag{3.22}$$

where $\boldsymbol{I}$ is the identity tensor. Since the fluid element is convected by the flow, the velocity gradient is time dependent even in steady flows; therefore the equation of motion (3.20) for the fluid element must be solved simultaneously to get $\nabla \boldsymbol{u}$. The lineal stretching is defined as

$$\lambda = \frac{|\mathrm{d}\boldsymbol{x}|}{|\mathrm{d}\boldsymbol{X}|}. \tag{3.23}$$

One characteristic of chaotic mixing is the exponential growth of the stretching with time, hence a timescale T_c could be found through

$$\langle \lambda \rangle = \exp\left(\frac{t}{T_c}\right), \tag{3.24}$$

where $\langle \lambda \rangle$ is a *geometric mean* of λ distributed over the whole flow domain.

In our implementation, initially a set of fluid particles was uniformly distributed within the (ξ, θ) domain, with each element containing four or nine fluid particles; then (3.20) and (3.22) were solved by the second-order Runge–Kutta method; the arithmetic mean over eight uniformly distributed orientations of the initial vector $\mathrm{d}\boldsymbol{X}$ and the geometric mean of λ over all the fluid samples were calculated at the end of each period; the effect on $\ln(\langle \lambda \rangle)$ of further increasing the number of orientations was found negligible.

3.6. *Search for periodic points*

The character of advective mixing produced by a time-periodic flow is determined by the location and character of the periodic points. The flow can be considered as a mapping M, in which each fluid particle gets mapped to a new position after each period T:

$$\boldsymbol{X}^{i+1} = M_T(\boldsymbol{X}^i). \tag{3.25}$$

A periodic point of n order is defined as

$$\boldsymbol{X}^n = \boldsymbol{X}^0 \quad \text{and} \quad \boldsymbol{X}^{i<n} \neq \boldsymbol{X}^0. \tag{3.26}$$

Periodic points are classified as either elliptic or hyperbolic depending on the nature of the deformation surrounding the material point, and this turns out to be determined by the eigenvalues of the linearized mapping in the neighbourhood of the point (see Ottino 1989).

Searching for the periodic points in the flow domain is not a simple task because, generally, the mapping cannot be analytically expressed and has to be obtained through the time integration of equation (3.20). For the creeping Newtonian and viscous shear-thinning flows, the velocity field is symmetric about the line through the two centres of the cylinders provided that the wave form of the cylinder rotation is symmetric. This symmetry is fully exploited by the investigations of Swanson & Ottino (1990) and Niederkorn & Ottino (1994) in which the task of two-dimensional searching can be reduced to a one-dimensional search on the line of symmetry. However, due to the fluid's memory, the symmetric property of the velocity field is lost in the corresponding viscoelastic flows. Here we propose an efficient two-dimensional searching algorithm which is an extension of the Newton iteration method for nonlinear equations.

Searching for the periodic points of n order is equivalent to finding the solution of the following equations:

$$x(X, Y) - X = 0, \quad y(X, Y) - Y = 0, \tag{3.27}$$

where (X, Y) is the initial position of a fluid particle and (x, y) is the position of the particle after n periods. This set of equations can be solved by Newton iteration in which the required differentials can be approximated by the finite differences. To avoid missing the periodic points, there should be a reasonably large number of initial particles distributed uniformly in the flow domain; most of them will diverge during the iteration, and only those which are sufficiently near a periodic

V_i	V_o	Interpolation order	NV	r.m.s error	Maximum error
−1	0	$P2$	10619	3.7×10^{-7}	1.0×10^{-6}
−1	0	$P3$	26159	1.0×10^{-7}	3.3×10^{-7}
−1	0	$P4$	48899	3.5×10^{-11}	1.9×10^{-10}
0	1	$P2$	10619	6.4×10^{-7}	1.8×10^{-6}
0	1	$P3$	26159	1.8×10^{-7}	4.6×10^{-7}
0	1	$P4$	48899	5.7×10^{-11}	4.0×10^{-10}

TABLE 1. Convergence with the interpolation orders. NV is the number of variables solved.

point will converge. In our implementation, both the initial and final positions were expressed in the bipolar coordinates (ξ, θ); the approximate differentials were taken as $\delta\xi = \delta\theta = 10^{-8}$. During the iteration process, a threshold value was set to exclude those points considered to be divergent. At the beginning, each element contained 16 points, and a total of 19 200 points participated in the mapping-iteration process; the number of the points was greatly reduced after each iteration due to the filtering procedure. With this scheme, we find that all the elliptic periodic points and most of the hyperbolic periodic points can be captured; occasionally, a few high-order hyperbolic periodic points could be missed, due to the large deformation near these hyperbolic points and also to the larger accumulating numerical errors in the higher-order mappings.

4. Solutions of steady flows

Chaotic advection provides a stringent test for numerically computed velocity fields: small errors in the velocity field will be swiftly magnified by the chaotic dynamics. Therefore it is necessary to estimate the error of the steady velocity fields. We define the maximum error and the root-mean-square (r.m.s) error as

$$\text{maximum error} = \max_1^n \sqrt{(\boldsymbol{u}_{analytic} - \boldsymbol{u}_{fe})^2},$$

$$\text{r.m.s.} = \sqrt{\frac{1}{n}\sum_1^n (\boldsymbol{u}_{analytic} - \boldsymbol{u}_{fe})^2},$$

where n is the number of nodes in the interior of the flow, $\boldsymbol{u}_{analytic}$ is the analytical solution of Wannier (1950), and $\boldsymbol{u}_{fe}$ is the finite element solution. It should be emphasized that, *in the case of Newtonian flow r.m.s. indicates the accuracy of a numerical solution, while in the case of viscoelastic or shear-thinning flows it can be used to evaluate the velocity deviations from the Newtonian flow*. Table 1 lists these two kinds of errors in our p-extension computations. The convergence with increasing interpolation orders is obvious and the convergence rate in terms of the number of variables solved is roughly exponential. In calculations $P2$ and $P3$ the interpolation orders were uniform throughout the whole mesh while in calculation $P4$ the interpolation of order –4 was only applied to four layers of the elements adjacent to the inner and outer cylinders.

In our computations of the steady flow with the UCM model, there seems no upper limit of the Deborah number when the inner cylinder is set rotating; however, the convergence of iteration was limited by $D_e = 6.5$ for the case of outer cylinder rotation. This is due to the very steep stress boundary layers developed near the inner cylinder

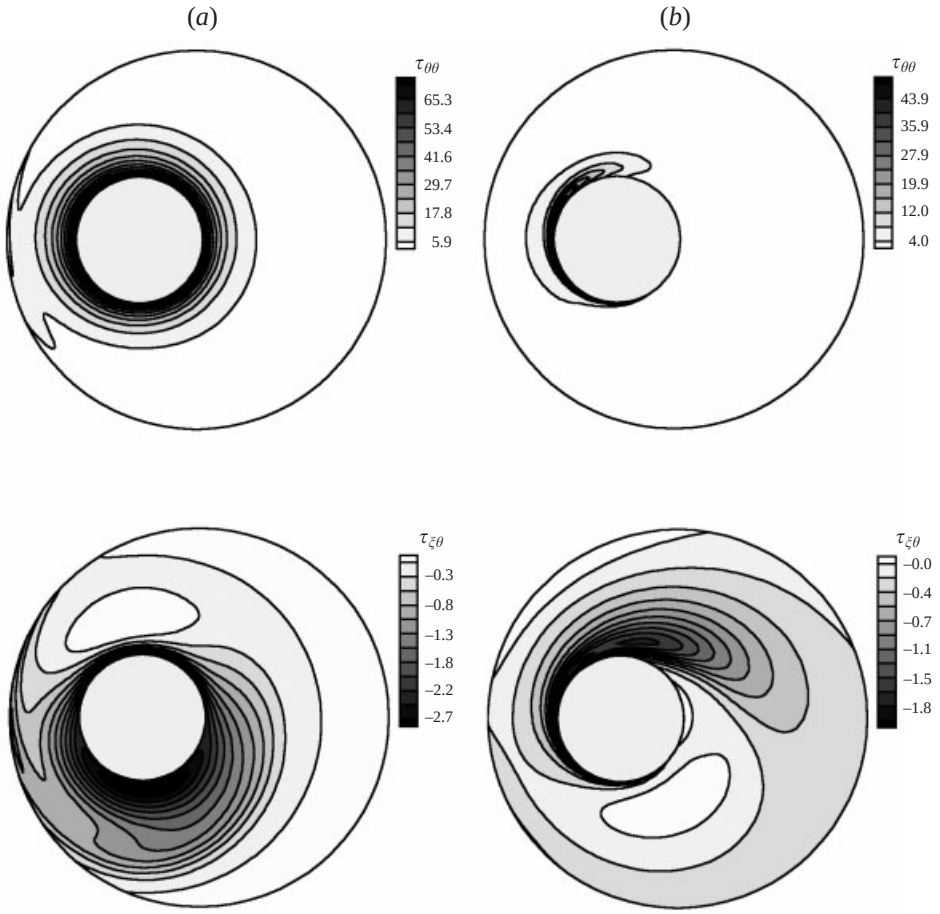

FIGURE 3. Contours of the stress components $\tau_{\xi\theta}$, $\tau_{\theta\theta}$ at $D_e = 6.0$; (*a*) the case of inner cylinder rotation, (*b*) the case of outer cylinder rotation.

V_i	V_o	D_e	r.m.s. deviation
-1	0	0.2	2.2×10^{-4}
-1	0	1.0	3.0×10^{-3}
-1	0	6.0	1.1×10^{-2}
0	1	0.2	6.8×10^{-4}
0	1	1.0	1.3×10^{-2}
0	1	6.0	1.4×10^{-1}

TABLE 2. R.m.s. velocity deviations of the UCM fluids from the Newtonian flow.

in the case of high D_e, which are difficult to resolve by the finite element mesh used. Figure 3 exhibits contours of the normal and shear stress components for the flows $D_e = 6.0$. In the literature, extensive numerical simulations of the viscoelastic flows between eccentric cylinders with small gap and low eccentricity have been reported. To validate our viscoelastic algorithm, we carried out calculations for UCM fluid in the case $\mu = 0.1, \epsilon = 0.1$ and compared the results with that of Beris, Armstrong

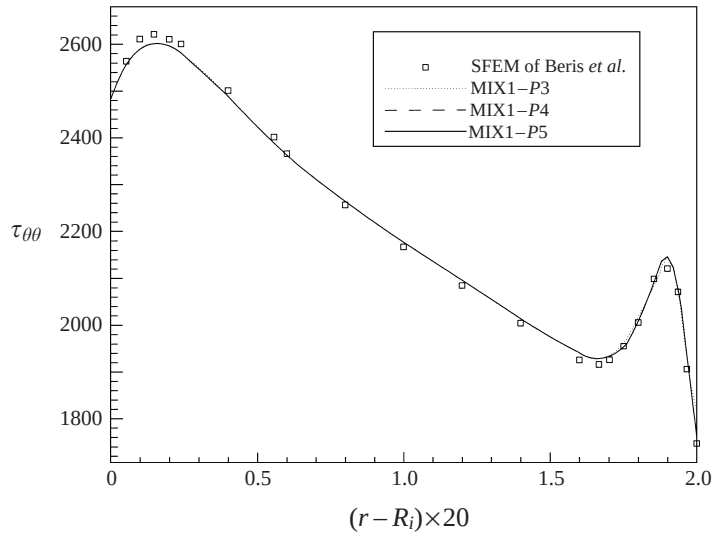

FIGURE 4. Results of the low-eccentricity case, $\mu = 0.1$, $\epsilon = 0.1$; the stress profile for $\tau_{\theta\theta}$ along the section $\theta = 3\pi/2$ for $D_e = 10$ in the cylindrical coordinate system centred at the inner cylinder.

& Brown (1987). They used a spectral finite element method (SFEM) in which the field variables were expanded by Fourier functions in the azimuthal direction and by the conventional finite element basis functions in the radial direction. This particular combination enabled them to use 200 elements in the radial direction. To date, the SFEM solution is still the most accurate one for this problem in the literature. Figure 4 plots the profiles of the normal stress $\tau_{\theta\theta}$ at $D_e = 10$; our calculations with only 12 radial elements exhibit an excellent p-convergence property and a good agreement with the SFEM solution. Note that this stress profile has also been confirmed by the computation of King *et al.* (1988) and by our previous computation using a cylindrical coordinate system (Fan *et al.* 1999).

To examine the impact of fluid elasticity on the steady velocity field, we choose the Deborah numbers of 0.2, 1.0, and 6.0 with the UCM model. Due to the difference in scaling, our case $D_e = 0.2$ is equivalent to the flow with Weissenberg number $We = 0.1$ studied by Niederkorn & Ottino (1993). Table 2 shows the r.m.s. velocity deviations of the UCM fluids from the analytical solution of the Newtonian fluid. For the shear-thinning fluids, we chose three pairs of the parameters in the Carreau model: $C_r = 10$ and $n = 0.9$, $C_r = 4$ and $n = 0.5$, $C_r = 10$ and $n = 0.3$. They span fluids having from weak to strong shear thinning. Table 3 shows the r.m.s. velocity deviations of the Carreau fluids from the analytical solution of the Newtonian fluid. The results in tables 2 and 3 indicate that the velocity deviation caused by fluid elasticity is much smaller than that caused by shear-thinning viscosity. It is worth mentioning that Niederkorn & Ottino's computations predict much larger velocity deviations for the UCM fluid; they treated the Newtonian flow as a limiting case of $D_e \to 0$ and gave the r.m.s. velocity deviations at $D_e = 0.002,\ 0.2$ to be 1.7×10^{-3} and 4.2×10^{-2}, respectively; the velocity deviations reported by them for the Carreau fluids are about $O(10^{-2})$ which is comparable with the values in table 3.

Figure 5 plots the streamlines of the UCM flows with $D_e = 0, 1, 6$. In the case of inner cylinder rotation, the recirculation zone slightly shrinks at $D_e = 1$ but then enlarges at $D_e = 6$; in the case of outer cylinder rotation, the recirculation zone

V_i	V_o	C_r	n	r.m.s. deviation
−1	0	10	0.9	2.0×10^{-2}
−1	0	4	0.5	1.4×10^{-1}
−1	0	10	0.3	2.8×10^{-1}
0	1	10	0.9	1.1×10^{-2}
0	1	4	0.5	6.3×10^{-2}
0	1	10	0.3	1.1×10^{-1}

TABLE 3. R.m.s. velocity deviations of the Carreau fluids from the Newtonian flow.

decreases monotonically, and at $D_e = 6$ the asymmetric pattern about the line of geometrical symmetry is obvious. The streamlines of the shear-thinning flows are plotted in figure 6. As the shear-thinning effect increases, the recirculation zone in the case of inner cylinder rotation shrinks, in agreement with the computation of Niederkorn & Ottino (1994). As expected, the velocity field is symmetric about the line of geometrical symmetry.

5. Results of piecewise-steady computations

5.1. *Mean lineal stretching*

With the procedure described in § 3.5, there are two factors that influence the accuracy of the stretching computation: the number of time steps per period, N_t, and the number of particle samples, N, used to model the spatial distribution of the stretching. We have tested the cases of $N_t = 6000$, $N = 4800$ and $N_t = 12\,000$, $N = 10\,800$; both of them are implemented with the analytical velocity field, and the case of $N_t = 6000$, $N = 4800$ is implemented with the finite element velocity with the interpolation order $P2$. Figure 7 demonstrates that the finite element solution is accurate enough and the lower numbers of time steps and fluid particles can faithfully predict the geometric mean of the spatially distributed stretching. It was noticed that if the arithmetic mean of λ is taken over the particle samples, the data are more scattered and less meaningful.

The fluid elasticity with the UCM model has little effect on the mean stretching. In figure 8, our calculations show that the stretching with $D_e = 0.2$ is the same as for the Newtonian fluid; for the case of $\theta = 3\pi/2$, the stretching with $D_e = 1.0$ and $D_e = 6.0$ is only slightly higher than for the Newtonian fluid; for the case of $\theta = 2\pi$, the stretching of the Newtonian fluid and of the UCM fluid with $D_e = 1.0$ are almost equal while that of the UCM fluid with $D_e = 6.0$ is slightly lower. These predictions disagree with Niederkorn & Ottino's computation. Instead of calculating the lineal stretching, they calculated the distance ratios of pairs of points initially separated by a small distance and observed that the separation ratios are compatible with the lineal stretching at early stages of the periodic flows. They predicted considerably smaller values of the geometric mean of the separation ratios for the UCM fluid with $D_e \leqslant 0.2$.

Figure 9 shows that the shear thinning has a great impact on the stretching and, for both types of boundary movement considered ($\theta = 3\pi/2$ and $\theta = 2\pi$), it reduces the mean stretching. The timescales T_c defined by equation (3.24) were deduced from a linear fitting to the data in figure 9. The effect of the shear thinning on the stretching can be quantified by a normalized time constant, $T_R = T_c/T_{c,Newtonian}$. For

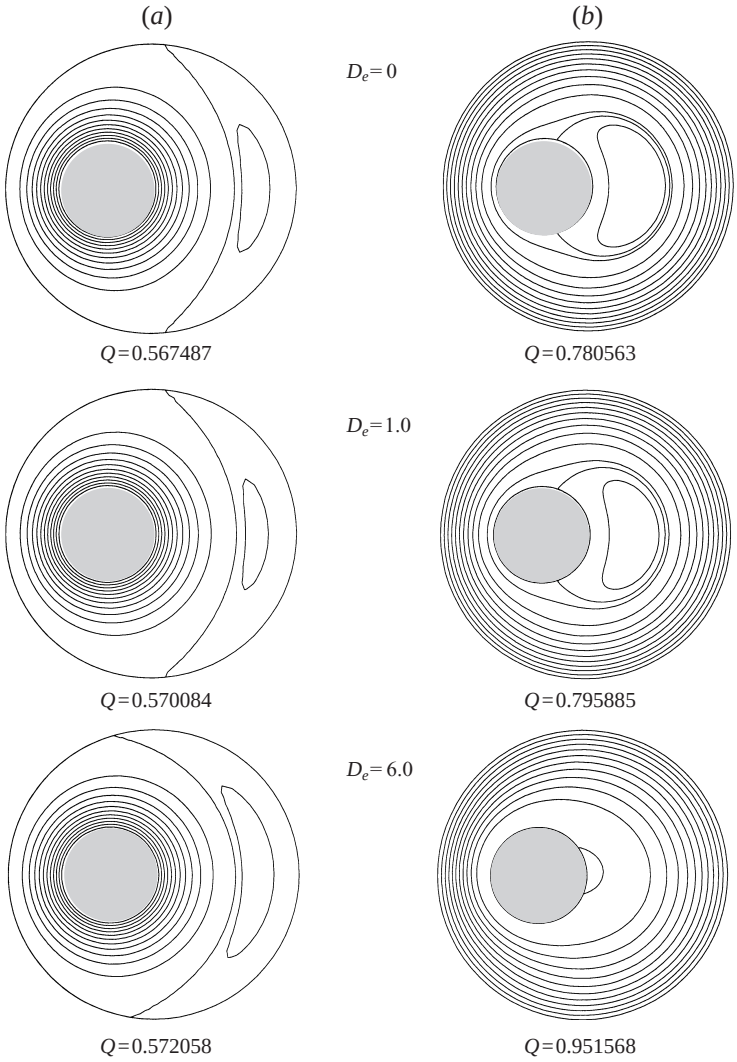

FIGURE 5. Streamline patterns of the Newtonian and UCM fluids; (*a*) the inner cylinder rotation, (*b*) the outer cylinder rotation; Q is the volumetric flux.

the Carreau fluid of $C_r = 4$ and $n = 0.5$ with the boundary movement of $\theta = 3\pi/2$, the computation of Niederkorn & Ottino (1994) gave $T_R \approx 1.08$ while our computation gives $T_R \approx 1.36$ indicating a much lower level of stretching; for the same Carreau fluid with the boundary movement of $\theta = 2\pi$, their prediction is $T_R \approx 0.95$ indicating a higher level of the stretching than the Newtonian fluid, while our result is $T_R \approx 1.07$.

5.2. *Advection of a passive tracer*

Figure 10 plots the advective coverages of a passive tracer after 16 periods for the rotation mode of $\theta = 3\pi/2$ and 12 periods for the rotation mode of $\theta = 2\pi$, respectively. The tracer structures of the Newtonian flow match very well with the experiments of Swanson & Ottino (1990) as well as with the computations of Niederkorn & Ottino (1993) using the analytical velocity field. As the elasticity level increases from $D_e = 0$ to $D_e = 1.0$, the tracer structure in the UCM fluid looks

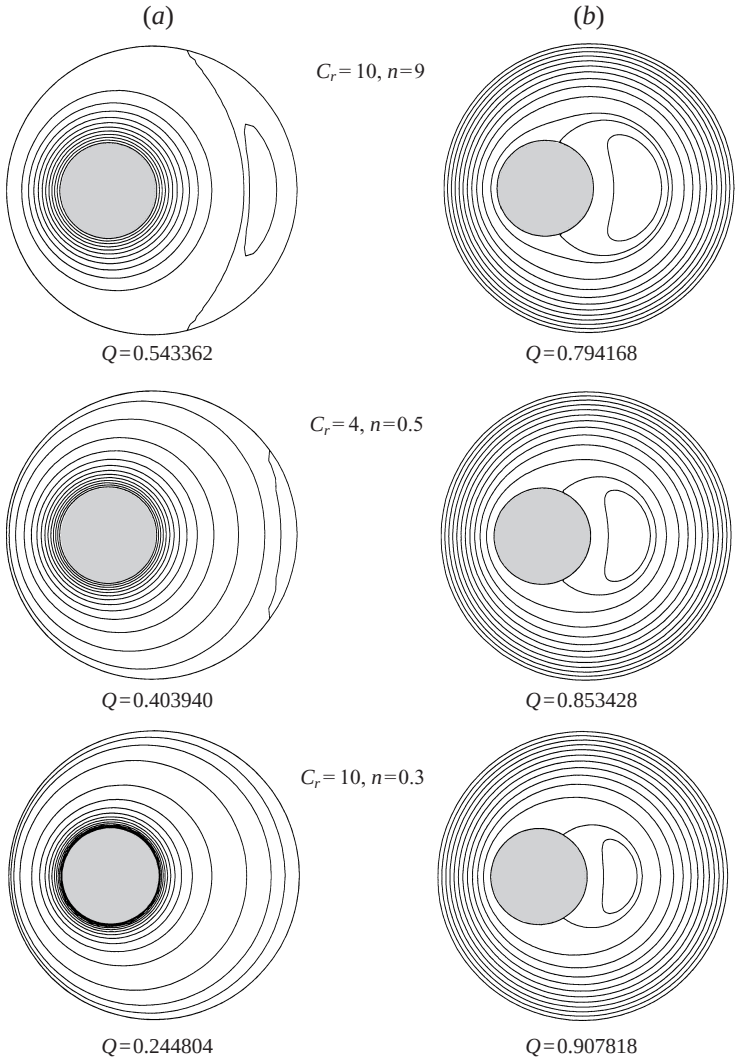

FIGURE 6. Streamline patterns of the Carreau fluids; (*a*) the inner cylinder rotation, (*b*) the outer cylinder rotation; Q is the volumetric flux.

indistinguishable from the Newtonian flow. On the contrary, the computation of Niederkorn & Ottino (1993) predicted dramatic changes of the tracer structure in the UCM fluid with the Deborah number as low as 0.08. The underlying cause for this discrepancy is that the steady velocity deviations of the UCM fluid computed by us are much smaller than theirs.

The shear-thinning property has a large impact on the advection of a passive tracer, as depicted in figure 11. The Carreau model with $C_r = 10$ and $n = 0.9$ represents a weak shear-thinning fluid in which a big island is formed in the middle of the large gap for $\theta = 3\pi/2$. At the medium level of shear thinning, $C_r = 4$ and $n = 0.5$, besides the further enlarged centre island, two symmetric side-islands and a small island in the small gap appear. For $\theta = 2\pi$, the crescent-shape island present in the Newtonian and the weak shear-thinning fluids has almost disappeared in the medium shear-thinning fluid. At the higher level of shear thinning, $C_r = 10$ and $n = 0.3$, the chaotic region has

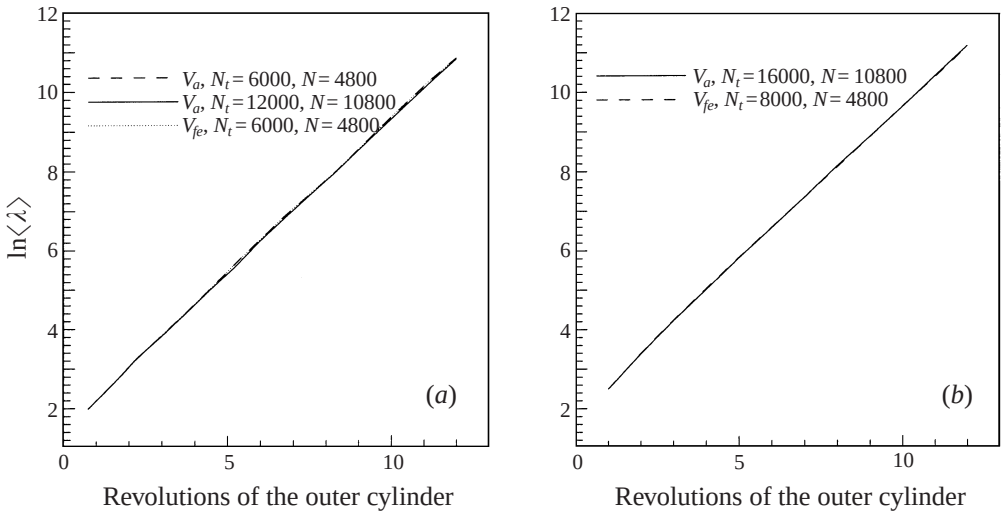

FIGURE 7. Logarithm of the geometrical mean stretching of the Newtonian fluid; V_a represents the analytical velocity field, V_{fe} the finite element solution with the interpolation order $P2$; N_t is the number of time steps for one period and N the number of fluid samples. (*a*) $\theta = 3\pi/2$, (*b*) $\theta = 2\pi$.

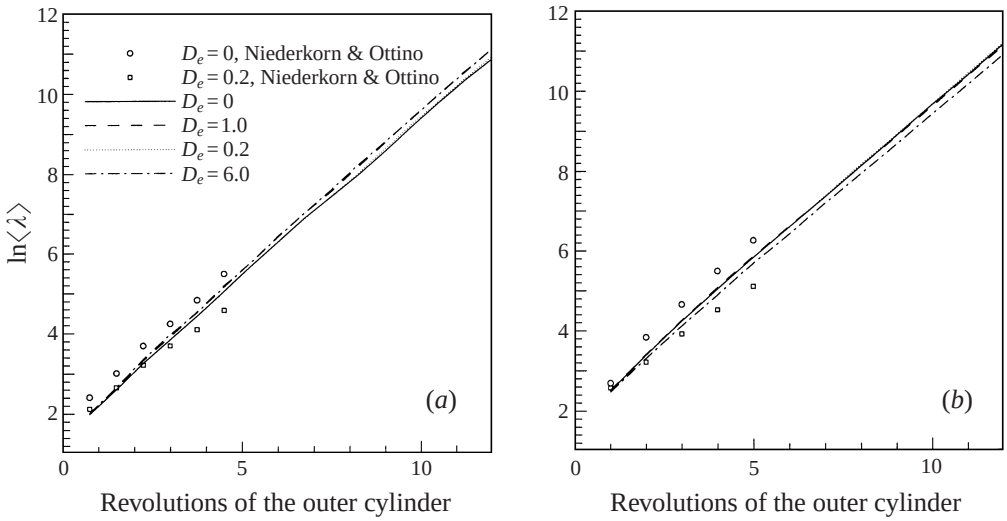

FIGURE 8. Logarithm of the geometrical mean stretching of the Newtonian and UCM fluids; the data of Niederkorn & Ottino represent the logarithm of the geometrical mean of the separation ratios. (*a*) $\theta = 3\pi/2$, (*b*) $\theta = 2\pi$.

greatly shrunk and the tracer seems to mainly follow several manifolds. Niederkorn & Ottino (1994) also calculated the flow for $C_r = 4$ and $n = 0.5$, and predicted no symmetric side-islands as seen in figure 11; this may partly explain why they obtained the stretching level considerably higher than ours for this flow.

5.3. *Periodic points*

First, we test the domain-search method described in § 3.6 on the Newtonian flow. For the rotation mode of $\theta = 2\pi$, we have compared the locations of the first-order periodic points found using the method and the finite element velocity field with

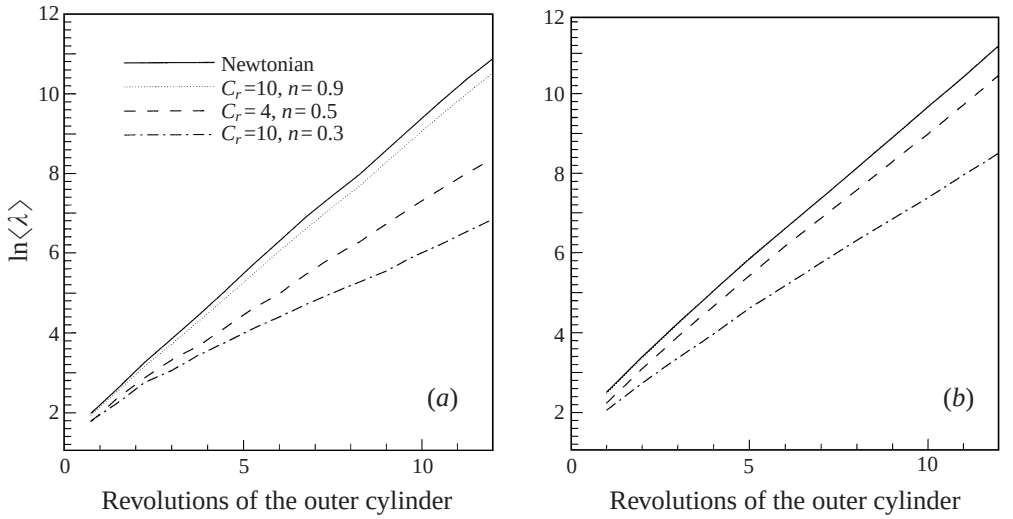

FIGURE 9. Logarithm of the geometrical mean stretching of the Newtonian and Carreau fluids. (*a*) $\theta = 3\pi/2$, (*b*) $\theta = 2\pi$.

x_{ref}	x_{fe}	y_{fe}	tr(J)	type
2.498903	2.498902	−0.000000	−8.30	hyperbolic
2.893627	2.893628	0.000000	13.80	hyperbolic
2.367330	2.367329	0.000000	31.36	hyperbolic
5.212781	5.212781	0.000000	−2.93	hyperbolic
5.315509	5.315510	0.000007	36.34	hyperbolic
6.049988	6.049991	−0.000000	−1.48	elliptic

TABLE 4. Locations of the periodic points of order-1 for the Newtonian fluids and $\theta = 2\pi$; these points are located on the symmetry line so $y = 0$; the subscript *ref* indicates the results of Souvaliotis *et al.* using the analytical solution and the line-searching scheme while *fe* indicates the results of the finite element solution with the interpolation order $P2$ and the domain-searching procedure.

those given by Souvaliotis *et al.* (1995) using a line-search method and the analytical velocity. The results are satisfactory: as listed in table 4, the location errors are within $O(10^{-6})$.

Due to the limitations of CPU time, we have only sought periodic points up to the second order. Figures 12 and 13 plot the locations of the periodic points computed by using the domain-search method and the finite element velocity fields of the second-order discretization. These periodic points are classified as hyperbolic or elliptic according to the eigenvalues of the Jacobian matrix of the mapping at that point; this in turn is determined by the trace of the Jacobian, tr(J): if $|\text{tr}(J)|$ is greater than 2 the point is hyperbolic, if less than 2 the point is elliptic; furthermore, for a hyperbolic point, a larger value of $|\text{tr}(J)|$ indicates a higher stretching along its unstable manifold; for an elliptic point, a smaller value of $|\text{tr}(J)|$ implies a more rotation-like mapping near that point.

We find it informative to follow the changes of the first-order periodic point A, and the second-order periodic points B, C, D, E, indicated on figures 13 and 14, and their traces of the Jacobian listed in table 5. For the Newtonian flow of $\theta = 3\pi/2$,

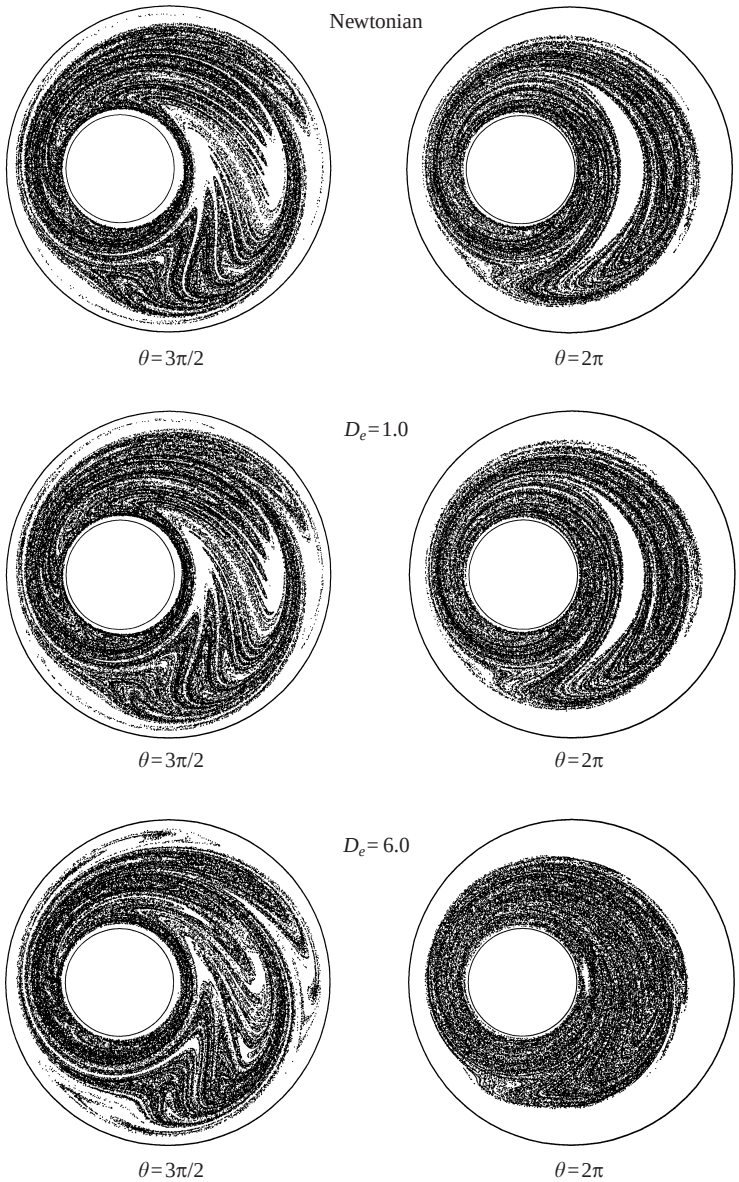

FIGURE 10. Advection of a passive tracer in the flows of the Newtonian and UCM fluids; the period number $N_p = 16$ for $\theta = 3\pi/2$ and $N_p = 12$ for $\theta = 2\pi$; piecewise-steady computations.

the intricate structure of the tracer folds in the large gap (see figure 10) is controlled by the hyperbolic first-order point A, and the two elliptic second-order points, B and C; their locations and characters have not changed noticeably at $D_e = 1.0$; however, at $D_e = 6.0$, the two elliptic points have been shifted closer to the hyperbolic point. Since the traces of the Jacobian approximate the critical value of -2, they are ready to be transformed into hyperbolic points; this corresponds to the near disappearing of the two islands in the large gap as depicted in figure 10, and to the higher mean stretching as shown in figure 8.

For the weak shear-thinning Carreau fluid, $C_r = 10$ and $n = 0.9$, since the trace of

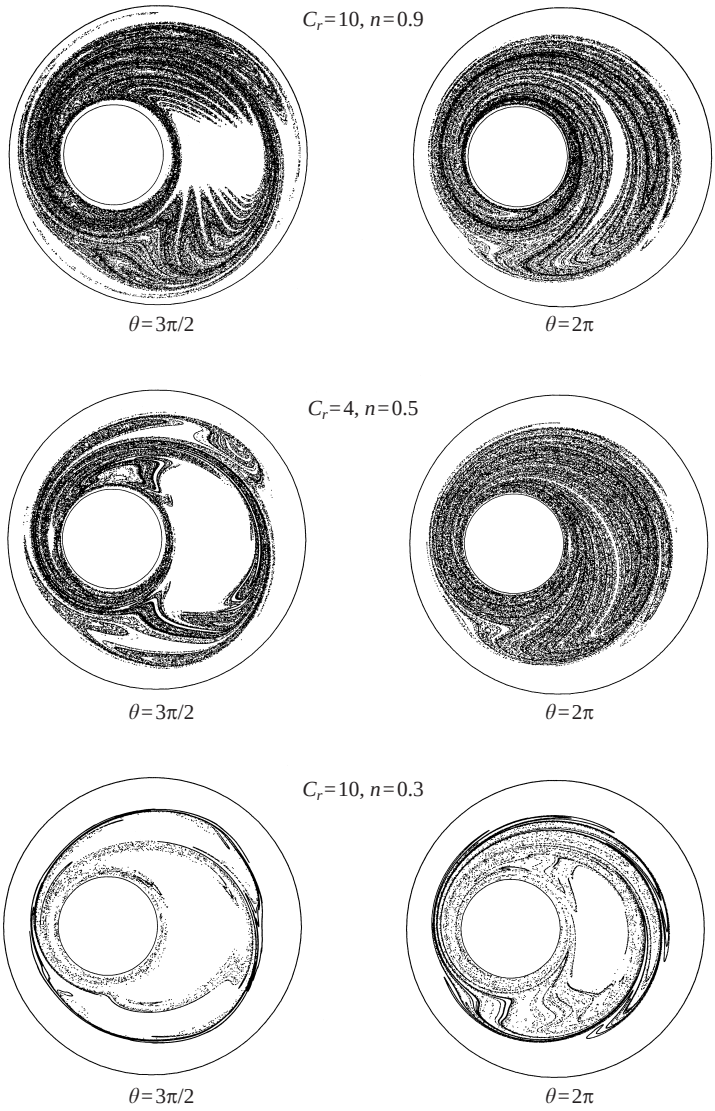

FIGURE 11. Advection of a passive tracer in the flows of the Carreau fluid; the period number $N_p = 16$ for $\theta = 3\pi/2$ and $N_p = 12$ for $\theta = 2\pi$; piecewise-steady computations.

$\theta = 3\pi/2$	$A(1)$	$B(2)$	$C(2)$	$D(2)$	$E(2)$
Newtonian	−2.12	−1.39	−1.39	−5.57	−5.51
$D_e = 1.0$	−2.16	−1.74	−1.74	−5.70	−5.70
$D_e = 6.0$	−2.43	−1.99	−1.99	−5.79	−5.79
$C_r = 10, n = 0.9$	−2.01	0.63	0.64	−4.45	−4.40
$C_r = 4, n = 0.5$	−1.38	* * **	* * **	−1.30	−1.28
$C_r = 10, n = 0.3$	−0.10	* * **	* * **	0.68	0.64

TABLE 5. Trace of the Jacobian, tr(J), of the periodic points in figures 13 and 14 where the number in brackets indicates the period order; the mode of boundary rotation is $\theta = 3\pi/2$.

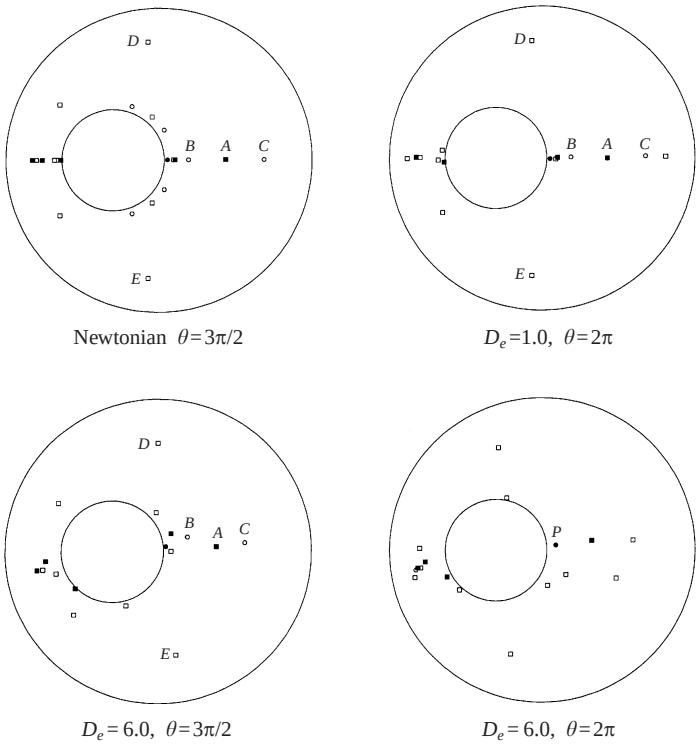

FIGURE 12. Locations of the periodic points for the Newtonian and UCM fluids; circle for the elliptic point, square for the hyperbolic point, filled for the period order 1 and open for the period order 2.

the Jacobian approximates the critical value, the point A is ready to be transformed into an elliptic point; meanwhile the elliptic character of points B and C is considerably stronger than that of the Newtonian flow; this corresponds to the large island in figure 11. For the medium shear thinning, $C_r = 4$ and $n = 0.5$, points A, B and C have collapsed into a single elliptic first-order periodic point; this corresponds to the further enlarged centre island in figure 11; moreover, the two original hyperbolic points, D and E, have been transformed into two elliptic points, resulting in two symmetric side-islands as plotted in figure 11; the presence of these islands gives rise to the considerably lower level of the mean stretching as shown in figure 9.

The elliptic first-order periodic point P in figure 12 is just located in the small island of the flow with $D_e = 6.0$ and $\theta = 2\pi$ as shown in figure 10. For the flow with $C_r = 4$ and $n = 0.5$ and $\theta = 3\pi/2$, the elliptic first-order periodic point F in figure 13 is located at the centre of the island in the small gap as shown in figure 11. Finally, the elliptic first-order periodic point Q in figure 13 ought to be responsible for the large island in the flow of $C_r = 10$ and $n = 0.3$ and $\theta = 2\pi$ as shown in figure 11.

6. Results of unsteady computations

As the fluid elasticity increases the transient process caused by the stress relaxation due to the rotation switches between the two cylinders should become more and more significant. Therefore it is reasonable to carry out a fully unsteady computation to examine the influence of the transient process on the advective mixing of the

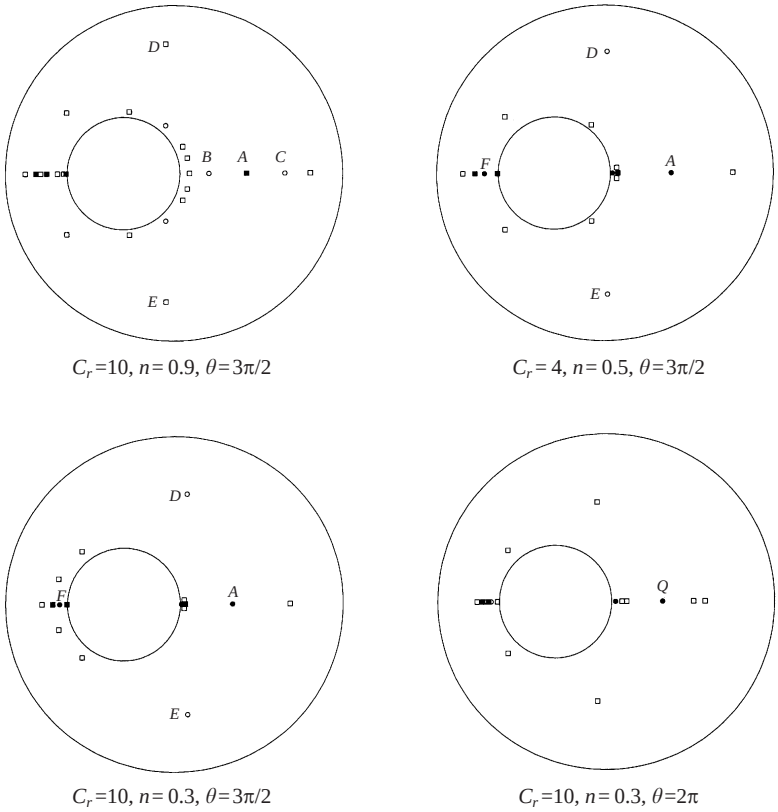

FIGURE 13. Locations of the periodic points for the Carreau fluid; circle for the elliptic point, square for the hyperbolic point, filled for the period order 1 and open for the period order 2.

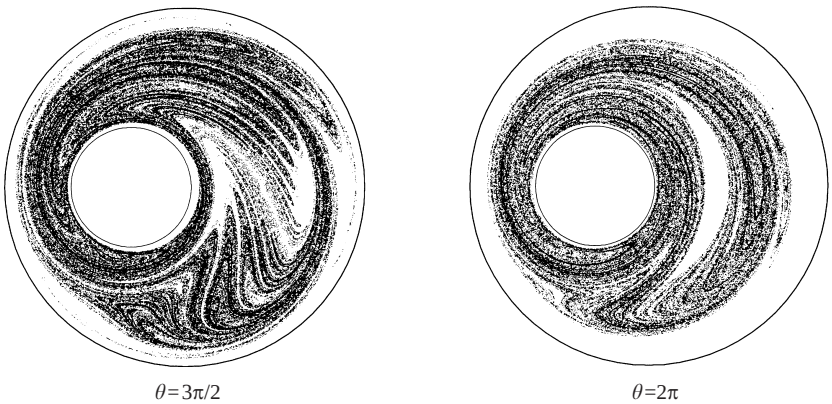

FIGURE 14. Advection of a passive tracer in the flows of the Oldroyd-B fluid with $D_e = 1.0$; the period number $N_p = 16$ for $\theta = 3\pi/2$ and $N_p = 12$ for $\theta = 2\pi$; unsteady computations.

viscoelastic flow, i.e. to check the piecewise-steady approximation. Due to the limitation of our unsteady algorithm, we have only carried out the simulations for the Oldroyd-B fluid, with a relative Newtonian viscosity of $\beta = 0.1$. With this small value of β, differences of the velocity fields between the Oldroyd-B and UCM fluids are expected to be insignificant. Actually, at $D_e = 0.2$, we found that the r.m.s. velocity

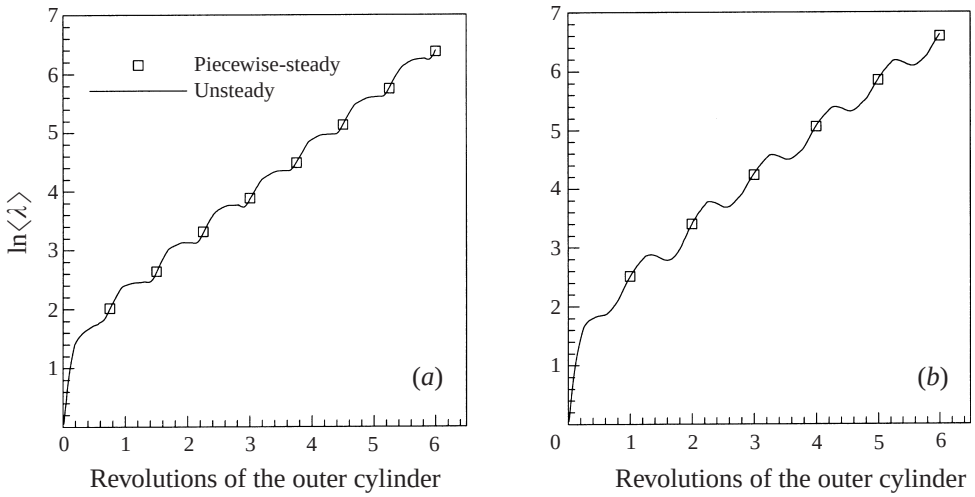

FIGURE 15. Logarithm of the geometrical mean stretching of the Oldroyd-B fluid with $D_e = 1.0$; comparison of the piecewise-steady and unsteady calculations. (*a*) $\theta = 3\pi/2$, (*b*) $\theta = 2\pi$.

differences between the Oldroyd-B and the UCM fluids are 2.3×10^{-5} and 6.8×10^{-5} for the inner and outer cylinder rotations, respectively. At $D_e = 1.0$, the corresponding r.m.s. differences are 4.1×10^{-4} and 1.5×10^{-3}.

In order to quantify the transient degree of the unsteady flow caused by sudden switches of the cylinder rotations, let us assume that if a variable's time rate of change (absolute value) is less than 0.001, it enters into a steady state. Thus, in a period of the flow, the unsteady calculation finishes when the maximum time rate of change of all variables is less than 0.001. Further we define the time fraction of the stress and time fraction of the velocity as

$$\varepsilon_s = \frac{T_s}{T}\,, \quad \varepsilon_v = \frac{T_v}{T},$$

where T_s is the maximum time period among all the stress components (including the pressure) required to reach the steady state and T_v is the corresponding time period for the velocity components, and T is the time period for the outer cylinder to rotate 2π. In a typical test, the flow was started from rest by a sudden step of rotation of the outer or inner cylinder; the unsteady computation for the Oldroyd-B fluid with $D_e = 0.2$ gave rise to $\varepsilon_s \approx 13\%$ and $\varepsilon_v \approx 4\%$, while the corresponding estimations for the unsteady flow with $D_e = 1.0$ are $\varepsilon_s \approx 69\%$ and $\varepsilon_v \approx 27\%$. Hence the transient degree of the velocity field is much less than the stress field.

Even with the improvements described in § 3.3, the unsteady algorithm is still excessively time consuming and a higher Deborah number demands a smaller time step to achieve computational stability. We have only calculated the cases $D_e = 0.2$ and $D_e = 1.0$. Quite unexpectedly, the advection of the passive tracer shows no significant changes in these unsteady viscoelastic computations. In figure 14 the tracer structures have no distinguishable character that is different from their counterparts in the piecewise-steady computations. We also found that the transient process has little effect on the geometric mean stretching. In figure 15 the stretching obtained from the unsteady computations for $D_e = 1.0$ closely follows the results of the corresponding piecewise-steady computations with only small oscillations. This behaviour can be explained by the following. Since the fluid inertia is neglected, the

velocity is determined only by the instantaneous state of the stress, i.e. at each time step the velocity field is quasi-steady. However, the elastic stress of the UCM fluid has relatively little effect on the velocity in steady flow, as indicated by our earlier computations.

7. Discussion

Niederkorn & Ottino's (1993) experiment with Boger fluids (elastic fluids with a constant viscosity) demonstrated that low elasticity ($D_e \leqslant 0.2$) considerably affects the asymptotic coverage of a dyed passive tracer. On the contrary, our computation for the UCM fluid shows that, up to $D_e = 1.0$, the advected coverage of a passive tracer is nearly indistinguishable from the Newtonian flow (using the Oldroyd-B model did not change the results). Upon inspection of the viscometric data of the fluids used by them, two possible reasons may be responsible for the disagreement. First, the first normal stress coefficient of their Boger fluids shows a strong shear-thinning behaviour while the UCM model predicts a constant first normal stress coefficient. Secondly, according to the data they presented, the viscometric tests were carried out only for the shear rate larger than $0.6\,\mathrm{s}^{-1}$ while they estimated that the actual shear rate in the mixing experiment was from 0.06 to $0.37\,\mathrm{s}^{-1}$. In this range of small shear rates, the rheological properties of the Boger fluids have not been measured with certainty, and the possibility of shear-rate dependence cannot be excluded. It is well known that at small Deborah numbers, the UCM model is equivalent to the second-order fluid whose constitutive equation is

$$\boldsymbol{\tau} = \dot{\gamma} - D_e \dot{\gamma}_{(1)},$$

where $\dot{\gamma}$ is the strain rate, $\dot{\gamma} = \nabla \boldsymbol{u} + \nabla \boldsymbol{u}^T$, and $\dot{\gamma}_{(1)}$ is the upper-convected derivative of $\dot{\gamma}$. The Tanner & Pipkin theorem (Bird *et al.* 1987; Tanner 1992; Huilgol & Phan-Thien 1997) states that the velocity field of a creeping plane flow of incompressible Newtonian fluids satisfies the equations for the flow of second-order fluid. We have carried out the computation for second-order fluid in the flow between eccentric cylinders, in which $\dot{\gamma}$ is treated as an additional independent variable and interpolated with the same order of polynomials as the velocity variable. The r.m.s. deviation of the velocity from the Newtonian analytical solution is 8.2×10^{-6} at $D_e = 0.2$ and 3.7×10^{-5} at $D_e = 1.0$, respectively. Next, we examine the influence of shear-thinning first normal stress by introducing a strain-rate-dependent Deborah number in the form similar to the Carreau model:

$$D_e = D_{e0}[1 + (C_r \dot{\gamma})^2]^{(n-1)/2},$$

where $\dot{\gamma} = \sqrt{(\frac{1}{2})II}$ and II is the second invariant of the strain rate $\dot{\gamma}$. Based on the viscometric data in the paper of Niederkorn & Ottino (1993) we chose the parameters $C_r = 10$ and $n = 0.4, 0.2$. We carried out the computation for the modified second-order fluid with $D_{e0} = 0.2$ and found that the r.m.s. deviations of the velocity from the Newtonian flow are at the same level as the UCM fluid with $D_e = 0.2$ listed in table 2, and the advection coverage of the passive tracer has no distinguishable difference from the Newtonian flow. To examine the effect of shear-thinning first normal stress at higher elasticity levels, the modified UCM model (MUCM) proposed by Apelian, Armstrong & Brown (1988) may be appropriate:

$$\boldsymbol{\tau} + \frac{D_e}{1 + (F \operatorname{tr}(\boldsymbol{\tau}))^{\alpha}} \boldsymbol{\tau}_{(1)} = (\nabla \boldsymbol{u} + \nabla \boldsymbol{u}^T),$$

where $\mathrm{tr}(\boldsymbol{\tau})$ is the trace of the extra-stress tensor $\boldsymbol{\tau}$, and F and α are two parameters. The MUCM model predicts a constant viscosity and a shear-thinning first normal stress difference which are controlled by F and α. We have computed the MUCM flow at $D_e = 1.0$ with the parameters $\alpha = 4.0$, $F = 0.1, 0.2$. The shear thinning of the first normal stress coefficient is significant; however, the major coverage structure of the advected passive tracer has not changed from the corresponding UCM flow. In summary, all our numerical tests seem to indicate that the dramatic changes of the tracer-advection pattern in Niederkorn & Ottino's experiment with the Boger fluids are probably caused by the non-constant viscosity instead of the fluid elasticity. In fact, if one inspects the tracer-coverage patterns in their experimental photographs and those of the weakly shear-thinning flow in figure 11, as well as those of the Carreau fluids computed by Niederkorn & Ottino (1994), one sees that some of them are qualitatively matched. However, the final decisive answer to whether small elasticity of the fluid has a large effect on the advective mixing of the flow between eccentric cylinders can only come from an experiment with more accurate rheological measurements.

Niederkorn & Ottino (1993) reported astonishingly good matches of the tracer-coverage structure between their experiment and computation using the UCM model. Generally, the Boger fluids are still very complex fluids and, to date, quantitative predictions for them in complex flows have not been achieved by numerical simulations using a constitutive equation with a single relaxation time. In their computations, the split-coefficient matrix (SCM) algorithm, originally developed for compressible gas flows, was employed to solve the field equations and, to make the set of governing equations hyperbolic, a small compressibility term in the continuity equation had to be introduced. The key point is the discretization error of the velocity field. They reported the r.m.s. error of 1.7×10^{-3} for the Newtonian flow with respect to the analytical solution and the r.m.s. velocity deviation of 4.2×10^{-2} for the UCM fluid with $D_e = 0.2$, while our corresponding computations are 3.7×10^{-7} and 2.2×10^{-4}, respectively. Therefore, it is very likely that the discretization errors in their computations have overwhelmed the physical velocity deviations of the viscoelastic flow from the Newtonian flow.

Obviously, a closely related problem is the magnitude of the velocity correction of the UCM fluid compared to that of the Newtonian fluid at a relatively low elasticity level, say $D_e = 0.2$. In this respect we wish to make a comment on the work of Kumar & Homsy (1996) on the chaotic advection of UCM fluid between slowly modulated eccentric cylinders. In order to determine the viscoelastic correction to the Newtonian flow field, they employed a semi-analytical method in which the velocity, pressure and stress are first expanded in powers of the Weissenberg number (equivalent to our definition of D_e); these expansions are then substituted into the field equations, truncated up to the terms of D_e^2. After some manipulations, they obtain the second-order correction equation of the stream function (the first-order correction is zero) and solve the equation by a finite difference technique. However, the range of validity, in terms of D_e, of their perturbation solutions is rather limited, even at a low value of $D_e = 0.2$. An implicit assumption in all perturbation methods is that the truncated terms are not significant relative to the terms which are kept.

In the perturbation solution presented in Kumar & Homsy (1996) for the case of $\Omega_2/\ \Omega_1 = -20$ and $e = 0.45$, where $\Omega_2/\ \Omega_1$ is the angular-velocity ratio of the inner and outer cylinders and e the eccentricity, the coefficient of the second-order correction for the volumetric flux is as high as 600 while the zeroth-order, Newtonian volumetric flux is 0.9; thus the second-order correction of $D_e = 0.2$ for the volumetric flux is 24, which is too large compared to the Newtonian volumetric

flux. We believe higher-order corrections need to be considered. In the analyses of the chaotic advection, they use the small eccentricity, $e = 0.1$, which has much smaller second-order corrections. But even in this case $D_e = 0.2$ and when $\Omega_2/\ \Omega_1 = -10$, the coefficient of the second-order correction is 7.3 (from their figure 5) while the corresponding Newtonian flux is about 0.4. Hence the second-order correction of the velocity at $D_e = 0.2$ is still relatively large compared with the Newtonian velocity field. Although Kumar & Homsy's work is valuable for understanding the mechanism of how viscoelasticity influences the advective mixing between eccentric cylinders, we believe that their perturbation solution can only apply at extremely small Deborah numbers.

8. Conclusions

We have studied numerically the viscoelastic effects on the chaotic mixing between alternately rotating eccentric cylinders. For the viscoelastic fluid modelled by the UCM constitutive equation, with the elasticity levels up to $D_e = 1.0$, our computations predict no noticeable changes of the mixing pattern of a passive tracer from the Newtonian flow. The stretching of the fluid elements, quantified by the geometrical mean of the spatial distribution, remains exponential up to $D_e = 6.0$, with only slight changes from the Newtonian flow. On the other hand, shear-thinning viscosity has a large impact on both the advection of a passive tracer and the mean stretching of the fluid elements. We have examined the influence of the shear-thinning first normal stress difference and discussed the causes for the discrepancy between our computation and Niederkorn & Ottino's experiment; the discussion leads to questioning whether small elasticity of the fluid has a large effect on the chaotic mixing in this periodic flow. The comparison between our computations and Niederkorn & Ottino's reveals the importance of reducing the discretization error in the computation of chaotic mixing.

In order to check the validity of the piecewise-steady assumption, an unsteady algorithm for creeping, viscoelastic flows has been developed and used to study the transient process of an Oldroyd-B fluid in this time-periodic flow. We have found that the transient period of the velocity is much shorter than the transient period of the elastic stress, and, up to $D_e = 1.0$, the advection of a passive tracer obtained with the piecewise-steady computation is almost unaffected by the unsteady computation, and the mean stretching computed by the unsteady method closely follows that computed by the piecewise-steady method with small oscillations. These behaviours can be attributed to the quasi-steady nature of the velocity field in creeping unsteady flows and to the relatively small effect of the elastic stress on the velocity in the steady flow between eccentric cylinders.

The characteristics of advective mixing produced by a time-periodic flow are controlled by the location and character of the periodic points. In the viscoelastic flows between eccentric cylinders, the distribution of the periodic points is not symmetric, hence we have developed a domain-search algorithm based on Newton iteration for locating the period points. Our computations have demonstrated that this algorithm is accurate and reasonably efficient. It is also satisfactory to have observed that the periodic points, found up to the second order, and their eigenvalues are indeed very informative in indicating the occurrence and location of islands (regular regions) among the chaotic region and in faithfully predicting the qualitative changes of the mean stretching of the fluid elements in this chaotic mixing flow.

We gratefully acknowledge the support from the Australian Research Council (ARC). Y. R. Fan also acknowledges the support of the National Natural Science Foundation of China. The computations were done on the Sydney Distributed Computing (SyDCom) Laboratory.

REFERENCES

Apelian, M. R., Armstrong, R. C. & Brown, R. A. 1988 Impact of the constitutive equation and singularity on the calculation of stick-slip flow: the modified upper-convected Maxwell mode (MUCM). *J. Non-Newtonian Fluid Mech.* **27**, 299–321.

Aref, H. & Balachandar, S. 1986 Chaotic advection in a Stokes flow. *Phys. Fluids* **29**, 3515–3521.

Behr, M. A., Franca, L. P. & Tezduyar, T. E. 1993 Stabilized finite element methods for the velocity-pressure-stress formulation of incompressible flows. *Comput. Meth. Appl. Mech. Engng* **104**, 31–48.

Beris, A. N., Armstrong, R. C. & Brown, R. A. 1987 Spectral/finite element calculations of the flow of a Maxwell fluid between eccentric rotating cylinders. *J. Non-Newtonian Fluid Mech.* **22**, 129–167.

Bird, R. B., Armstrong, R. C. & Hassager, O. 1987 *Dynamics of Polymer Liquids, I: Fluid Mechanics*, 2nd edn. Wiley.

Brooks, A. N. & Hughes, T. J. R. 1982 Streamline upwind Petrov-Galerkin method for convection dominated flows with particular emphasis on the incompressible Navier–Stokes equation. *Comput. Meth. Appl. Mech. Engng* **32**, 199–259.

Chaiken, J., Chu, C. K., Tabor, M. & Tan, M. 1987 Lagrangian turbulence and spatial complexity in a Stokes flow. *Phys. Fluids* **30**, 687–694.

Fan, Y. R. 1997 A comparative study of the discontinuous Galerkin and continuous SUPG finite element methods for computation of viscoelastic flows. *Comput. Meth. Appl. Mech. Engng* **141**, 47–65.

Fan, Y. R. & Crochet, M. J. 1995 High-order finite element methods for steady viscoelastic flows. *J. Non-Newtonian Fluid Mech.* **57**, 283–311.

Fan, Y. R., Tanner, R. I. & Phan-Thien, N. 1999 Galerkin/least-square finite element methods for steady viscoelastic flows. *J. Non-Newtonian Fluid Mech.* **84**, 233–256.

Franjione, J. G. & Ottino, J. M. 1987 Feasibility of numerical tracking of material lines and surfaces in chaotic flows. *Phys. Fluids* **30**, 3641–3643.

Franca, L. P. & Frey, S. L. 1992 Stabilized finite element methods: II. the incompressible Navier–Stokes equations. *Comput. Meth. Appl. Mech. Engng* **99**, 209–233.

Guénette, R. & Fortin, M. 1995 A new mixed finite element method for computing viscoelastic flows. *J. Non-Newtonian Fluid Mech.* **60**, 27–52.

Hughes, T. J. R., Franca, L. P. & Hublert, G. M. 1989 A new finite element formulation for computational fluid dynamics: VIII. the Galerkin/least-square method for advective-diffusive equations. *Comput. Meth. Appl. Mech. Engng* **73**, 173–189.

Huilgol, R. R. & Phan-Thien, N. 1997 *Fluid Mechanics of Viscoelasticity*. Elsevier.

Kaper, T. J. & Wiggins, S. 1993 An analytical study of transport in Stokes flows exhibiting large-scale chaos in the eccentric journal bearing. *J. Fluid Mech.* **253**, 211–243.

King, R. C., Apelian, M. R., Armstrong, R. C. & Brown, R. A. 1988 Numerically stable finite element techniques for viscoelastic calculations in smooth and singular geometries. *J. Non-Newtonian Fluid Mech.* **29**, 147–216.

Kumar, S. & Homsy, G. M. 1996 Chaotic advection in creeping flow of viscoelastic fluids between slowly modulated eccentric cylinders. *Phys. Fluids* **8**, 1774–1787.

Kusch, H. A. & Ottino, J. M. 1992 Experiments on mixing in continuous chaotic flows. *J. Fluid Mech.* **236**, 319–348.

Muzzio, F. J., Swanson, P. D. & Ottino, J. M. 1991 The statistics of stretching and stirring in chaotic flows. *Phys. Fluids* A **3**, 822–834.

Niederkorn, T. C. & Ottino, J. M. 1993 Mixing of a viscoelastic fluid in a time-periodic flow. *J. Fluid Mech.* **256**, 243–268.

Niederkorn, T. C. & Ottino, J. M. 1994 Chaotic mixing of shear-thinning fluids. *AIChE J.* **40**, 1782–1793.

Ottino, J. M. 1989 *The Kinematics of Mixing: Stretching, chaos, and Transport*. Cambridge University Press.

Rajagopalan, D., Armstrong, R. C. & Brown, R. A. 1990 Finite element methods for calculations of steady viscoelastic flow using constitutive equations with a Newtonian viscosity. *J. Non-Newtonian Fluid Mech.* **36**, 159–192.

Souvaliotis, A., Jana, S. C. & Ottino, J. M. 1995 Potentialities and limitations of mixing simulations. *AIChE J.* **41**, 1605–1621.

Sun, J., Phan-Thien, N. & Tanner, R. I. 1996 An adaptive viscoelastic stress splitting scheme and its applications: AVSS/SI and AVSS/SUPG. *J. Non-Newtonian Fluid Mech.* **65**, 75–91.

Swanson, P. D. & Ottino, J. M. 1990 A comparative computational and experimental study of chaotic mixing of viscous fluids. *J. Fluid Mech.* **213**, 227–249.

Szabo, B. & Babuska, I. 1991 *Finite Element Analysis*. John Wiley & Sons.

Talwar, K. K. & Khomami, B. 1992 Application of higher order finite element methods for viscoelastic flows in porous media. *J. Rheol.* **36**, 1377–1416.

Tanner, R. I. 1992 *Engineering Rheology*, Revised edn. Oxford University Press.

Wannier, G. H. 1950 A contribution to the hydrodynamics of lubrication. *Q. Appl. Maths* **8**, 1–32.

Warichet, V. & Legat, V. 1997 Adaptive high-order prediction of the drag correction factor for the upper-convected Maxwell fluid. *J. Non-Newtonian Fluid Mech.* **73**, 95–114.